

Electrical and Structural Dual Function of Oxygen Vacancies for Promoting Electrochemical Capacitance in Tungsten Oxide

Zi-Hang Huang, Hao Li, Wen-Han Li, Graeme Henkelman, Baohua Jia, and Tianyi Ma*

Intrinsic defects, including oxygen vacancies, can efficiently modify the electrochemical performance of metal oxides. There is, however, a limited understanding of how vacancies influence charge storage properties. Here, using tungsten oxide as a model system, an extensive study of the effects of structure, electrical properties, and charge storage properties of oxygen vacancies is carried out using both experimental and computational techniques. The results provide direct evidence that oxygen vacancies increase the interlayer spacing in the oxide, which suppress the structural pulverization of the material during electrolyte ion insertion and removal in prolonged stability tests. Specifically, no capacitive decay is detected after 30 000 cycles. The medium states and charge storage mechanism of oxygen-deficient tungsten oxide throughout electrochemical charging/discharging processes is studied. The enhanced rate capability of the oxygen-deficient WO_{3-x} is attributed to improved charge storage kinetics in the bulk material. The WO_{3-x} electrode exhibits the highest capacitance in reported tungsten-oxide based electrodes with comparable mass loadings. The capability to improve electrochemical capacitance performance of redox-active materials is expected to open up new opportunities for ultrafast supercapacitive electrodes.

eco-friendliness, and low cost. Metal oxides are also important as electrode materials for energy storage.^[1] However, mild reaction kinetics and low conductivity of pristine metal oxide electrodes resulting in severe capacitance loss, which limit their practical use as electrodes for ultrafast supercapacitors.^[2] The conductivity relies critically on the carrier density of n-type metal oxide semiconductors.^[3] The concentration of stoichiometric defects will directly affect the carrier density of metal oxides.^[4] In short, the band bending at the semiconductor/electrolyte junction is improved owing to enhanced carrier density, thereby promoting charge transportation.^[5] Therefore, the electrical conductivity and reaction kinetics of metal oxides is substantially improved. Our ability to manufacture oxygen-defective metal oxide nanostructures with elevated donor densities provides fresh possibilities to address this long-lasting challenge.^[6] For example, Lu's group reported a supercapacitor assembled by an


1. Introduction

Metal oxides have numerous positive attributes as functional materials, including a high natural abundance, easy synthesis,

oxygen-deficient manganese dioxide nanorod that shows a large capacitance (449 F g^{-1}) and outstanding cycling stability.^[6d] In an oxygen-defective hematite, synthesized by modifying the oxygen content, the issue of poor iron oxide conductivity is also optimized.^[6b] However, the impact of oxygen vacancies on improving electrochemical property of metal oxides for energy storage applications is still limited.

Dr. Z.-H. Huang, W.-H. Li
Institute of Clean Energy Chemistry
Key Laboratory for Green Synthesis and Preparative Chemistry
of Advanced Materials
College of Chemistry
Liaoning University
Shenyang 110036, China
Dr. H. Li, Prof. G. Henkelman
Department of Chemistry
The Oden Institute for Computational Engineering and Sciences
The University of Texas at Austin
105 E. 24th Street, Stop A5300, Austin, TX 78712, USA
Prof. B. Jia, Prof. T. Ma
Centre for Translational Atomaterials, Faculty of Science
Engineering and Technology
Swinburne University of Technology
Hawthorn, VIC 3122, Australia
E-mail: tianyima@swin.edu.au

Another challenge that continues to plague metal oxides is their electrochemical instability, which is largely due to chemical dissolution, phase transitions, and structural comminution.^[7] Charge accumulation in accompany with ion intercalation and de-intercalation modify the crystal structure and surface morphology of metal oxides. Repeated charging and discharging induces considerable structural deformation, resulting in electrode deterioration and capacitance reduction.^[6b,7a] In recent studies, oxygen-defective metal oxides have been discovered to have outstanding electrochemical stabilization.^[6a,b,d,8] Dunn's group found that introducing oxygen vacancies in MoO_3 helps to preserve the structure throughout insertion/extraction of Li ions, which enables excellent cycling performance.^[7c] Taken together, oxygen vacancies could be a leading role in modulating the structural and electrical properties of metal oxides. Moreover, medium states in such oxygen-defective metal oxides throughout charging/discharging are

 The ORCID identification number(s) for the author(s) of this article can be found under <https://doi.org/10.1002/sml.202004709>.

DOI: 10.1002/sml.202004709

still uncertain. Studies of the relationship between the nature of oxygen vacancies and metal oxide electrochemical stabilization are important to understand the ability of oxygen-deficient metal oxides for electrochemical energy storage.

Herein, we demonstrate the function of oxygen vacancies in a WO_3 model system to enhance its performance for energy storage applications. Theoretical calculations (density functional theory) provide insights on the formation of oxygen vacancy sites and structural properties for oxygen-deficient WO_3 . A high loading (77 mg cm^{-2}) of oxygen-deficient WO_3 nanowire (NW) delivers an excellent capacitance of 4.76 F cm^{-2} at 3 mA cm^{-2} , and maintains 2.49 F cm^{-2} at 40 mA cm^{-2} . To the best of our knowledge, such performance of synthesized oxygen-deficient WO_3 NW material, is at the top of the reported tungsten oxide-based electrodes.

2. Results and Discussion

2.1. Materials Characterization and Theoretical Calculations

Oxygen-deficient WO_{3-x} was prepared by a seed-assisted hydrothermal synthesis (Experimental Section). To elucidate the crystalline structure and morphology of the oxygen-deficient WO_{3-x} , various electron microscopy characterizations were performed. The SEM image in **Figure 1a** indicates that WO_{3-x} material is of a radial nanowire structure. The inset in **Figure 1a** shows a TEM image of an isolated nanowire, revealing its uniform diameter of $\approx 100 \text{ nm}$. The enlarged image shows disordered structures on the edge of WO_{3-x} nanowire, identified on the basis of lattice disappearance (**Figure 1b**), indicating a large number of surface defects.^[9] The energy-dispersive

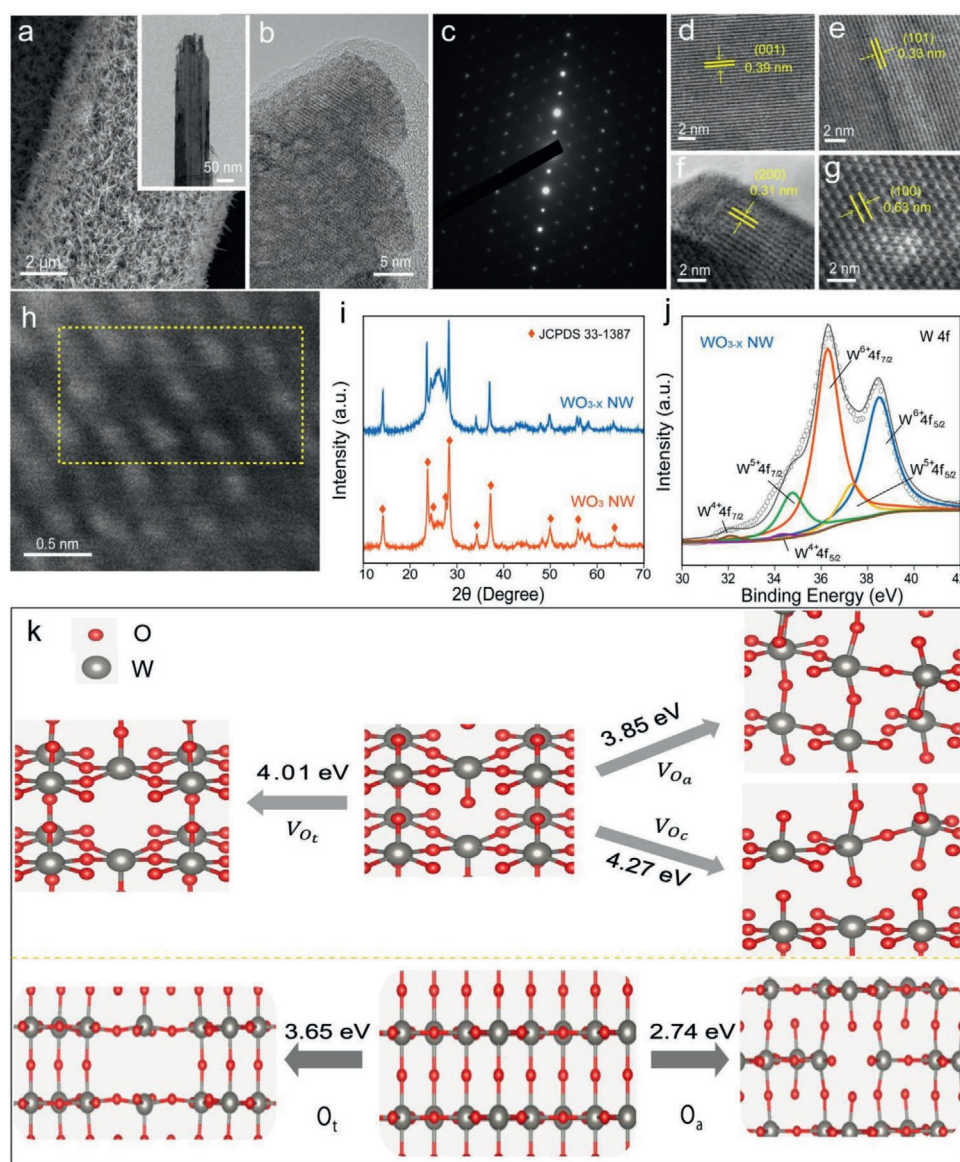


Figure 1. a) SEM and TEM images of WO_{3-x} NW. b) HRTEM image and c) the corresponding SAED pattern of WO_{3-x} NW. d–g) Magnified HRTEM images of WO_{3-x} . h) Atomic resolution TEM image of WO_{3-x} . i) XRD patterns of WO_{3-x} NW and WO_3 NW. j) Core level W 4f XPS spectra of WO_{3-x} NW. k) DFT optimized structures of WO_3 and WO_{3-x} . O_a , O_c , and O_t represent the vacancies of oxygen in different sites. The upper and lower panels represent orthorhombic and hexagonal structures, respectively. Red and grey spheres represent O and W, respectively.

X-ray spectroscopy (EDS) elemental mappings reveal the uniform distribution of all elements in oxygen-deficient WO_{3-x} (Figure S1, Supporting Information). To quantify the elements ratio (W/O) of WO_{3-x} and WO_3 NWs, EDS spectra was performed. As shown in Figure S2, Supporting Information, the elements ratio (W/O) of WO_{3-x} and WO_3 NWs are 1:2.82 and 1:3.05, respectively. Additionally, the bright and ordered diffraction spots in the SAED pattern shows the single crystalline nature of nanowire (Figure 1c). As measured, the distinct lattice fringe spacings of ≈ 0.39 , 0.33, 0.31, and 0.63 nm can be observed in the enlarged high-resolution TEM image for WO_{3-x} sample (Figure 1d–g), consistent with the (001), (101), (200), and (100) planes of WO_3 (JCPDS No. 33–1387).^[7a] The oxygen-deficient WO_{3-x} nanowire structure is further confirmed by atomic resolution TEM imaging as shown in Figure 1h. As well as surface defects, WO_{3-x} also has planar defects, as evidenced by the missing lattice fringes with sizes of 0.3–0.5 nm in the atomic-resolution image. These findings show that oxygen vacancies are not restricted to the external surface, but rather extend throughout the material. Figure 1i collects the XRD pattern of the material (blue). The peaks correspond to WO_3 structure consistent with JCPDS No. 33–1387.^[7a,10] Normally, WO_3 is yellow in color, so amazingly, the as-synthesized electrode color was purplish blue (Figure S3a, Supporting Information). This condition shows that the as-synthesized WO_3 was reduced in the process of synthesis treatment. For comparison, the oxygen-deficient WO_{3-x} NW was subjected to heat treatments to completely oxidize the WO_{3-x} . After heat treatment, the color of the sample turned yellow and the phase, which corresponded to the WO_3 structure, was confirmed by XRD (Figure 1i). No significant change was apparent from SEM in the NW morphology (Figure S3b, Supporting Information).

The oxygen vacancy concentration and the oxidation state of the oxygen-deficient WO_{3-x} NW and WO_3 NW were analyzed using X-ray photoelectron spectroscopy (XPS). The spectrum of the XPS surveying illustrates that the samples have three components (W, O, and C elements) without any other sensitive impurities (Figures S4, S5, Supporting Information). The composition of the oxygen-deficient WO_{3-x} NW corresponds to $\text{WO}_{2.73}$ based on the tungsten and oxygen XPS peak areas. The W 4f core level (Figure 1j and Figure S6, Supporting Information) manifests two well-defined peaks centered at 36.28 and 38.50 eV, respectively, corresponding to W^{6+} in tungsten oxides.^[11] Notably, in comparison to WO_3 , two different peaks are observed, at lower binding energies of 34.75 and 37.33 eV, which correlate to the W^{5+} state.^[12] Two peaks at 32.10 and 34.30 eV were assigned to the W^{4+} state.^[13] The peak area ratio of W 4f_{7/2} and W 4f_{5/2} peaks for W^{6+} , W^{5+} , W^{4+} , are summarized in Table S1, Supporting Information. The XPS results confirm the existence of oxygen vacancies in oxygen-deficient WO_{3-x} . These defects would improve the carrier density of metal oxides, which can promote charge transportation and reaction kinetics in thick electrode materials, resulting in enhanced charge storage capacity.

To understand the electrical features of oxygen-deficient WO_{3-x} NW that influence and determine its properties, electrochemical impedance measurements were conducted. The Mott–Schottky approach is an excellent method to study the electrical properties of the Schottky barrier formed between

the electrolyte and a semiconductor material.^[6a] As shown in Figure S7, Supporting Information, capacitances are derived from the electrochemical impedance obtained at 10 kHz frequency in the dark. Oxygen-deficient WO_{3-x} and WO_3 NW electrodes in Mott–Schottky plots display positive slope, showing the features of n-type semi-conductor. The carrier densities of the WO_3 and WO_{3-x} NWs are calculated to be 9.9×10^{19} and $2.3 \times 10^{22} \text{ cm}^{-3}$, respectively (by the Mott–Schottky equation, as shown in the Supporting Information). As expected, oxygen-deficient WO_{3-x} NW electrode shows an increase in carrier density in three orders of magnitude compared to WO_3 . The improved carrier density in WO_{3-x} NW can be attributed to the oxygen vacancies, which are known to be electron donors in WO_{3-x} .^[14] To further characterize the accessible surface area, N_2 adsorption-desorption measurements were conducted on WO_{3-x} NW and WO_3 samples (Figure S8, Supporting Information). N_2 gas adsorption-desorption isotherm analysis reveals that oxygen-deficient WO_{3-x} NW displayed a large surface area than that of the fully oxidized WO_3 NW. This is helpful to promote effective contact with electrolyte and enhance the electrochemical reaction for energy storage. Methylene blue (MB) UV-spectrum also show that the oxygen-deficient WO_{3-x} NW exhibit slightly increased ion accessible surface area (Figure S9, Supporting Information).

To understand the formation of oxygen vacancies in tungsten oxide, a previous density functional theory (DFT) study on a monoclinic WO_3 structure has shown the coexistence of W^{4+} , W^{5+} , and W^{6+} in monoclinic WO_{3-x} under mild temperature conditions.^[15] The monoclinic and orthorhombic structures are the most favorable structures of WO_3 under mild conditions and the hexagonal WO_3 has the same W-O ordering.^[16] Meanwhile, XRD results indicated a possible predominated hexagonal WO_3 structure from our experiments (Figure 1i). Therefore, we performed DFT calculations to understand the formation of oxygen vacancies in both hexagonal and orthorhombic WO_3 structures and we hoped to provide a generalized guideline from theory in the conclusion.^[17] Our calculated formation energies (in the form of enthalpy) for an oxygen vacancy in different oxygen sites are shown in Figure 1k. According to the orientation of oxygen ordering, the type of oxygen vacancy in a WO_3 can be classified as O_a , O_c , or O_t .^[7c] It was found from the orthorhombic structure that the configuration with a formation energy of 4.01 eV corresponds to an oxygen vacancy at the O_t site, while the vacancies at the O_a and O_c sites have formation energies of 3.85 and 4.27 eV (Figure 1k).^[15] As for the hexagonal WO_3 structure, the vacancy formation of O_a (2.74 eV) also has a slightly lower formation energy than O_t (3.65 eV), indicating a similar phenomenon. Chatten et al. have discussed that a pair of W^{5+} ions is likely to form in a defect center of WO_3 .^[17] However, due to the high formation energy for all the oxygen vacancies in our DFT calculations, we expect that W^{6+} is predominant as compared to W^{5+} , in good agreement with our experimental observation (Figure 1j). Since the hexagonal, monoclinic, and orthorhombic structures are expected to coexist at our experimental temperature, due to the similar formation energies,^[17] it is not surprising to see a coexistence of W^{4+} , W^{5+} , and W^{6+} in our XPS results with the intensity order of $\text{W}^{6+} > \text{W}^{5+} > \text{W}^{4+}$ (Figure 1j).

2.2. Electrochemical Valuation

To comprehend oxygen vacancies on electrochemical behavior, galvanostatic charge–discharge (GCD) and cyclic voltammetry (CV) experiments were performed in 0.5 M H₂SO₄ electrolyte. A significant increase of current density is observed after the carbon cloth is covered by tungsten oxide, due to the additional pseudocapacitance provided by the high-loading tungsten oxide (Figure S10, Supporting Information). As shown in Figure 2a, while both oxygen-deficient WO_{3-x} and WO₃ NW electrodes

display pseudocapacitive behavior with a sequence of broad peaks that can be connected to the transformation between different valence states. The CV profile of oxygen-deficient WO_{3-x} NWs presents increased current compared with WO₃ in the full potential range, which exhibits higher capacitive performance. The GCD profiles of the samples collected at 10 mA cm⁻² are given in Figure 2b, and those measured at current densities between 3 and 40 mA cm⁻² are displayed in Figure S11, Supporting Information. The oxygen-deficient WO_{3-x} electrode, which shows an extended discharge time, further demonstrates

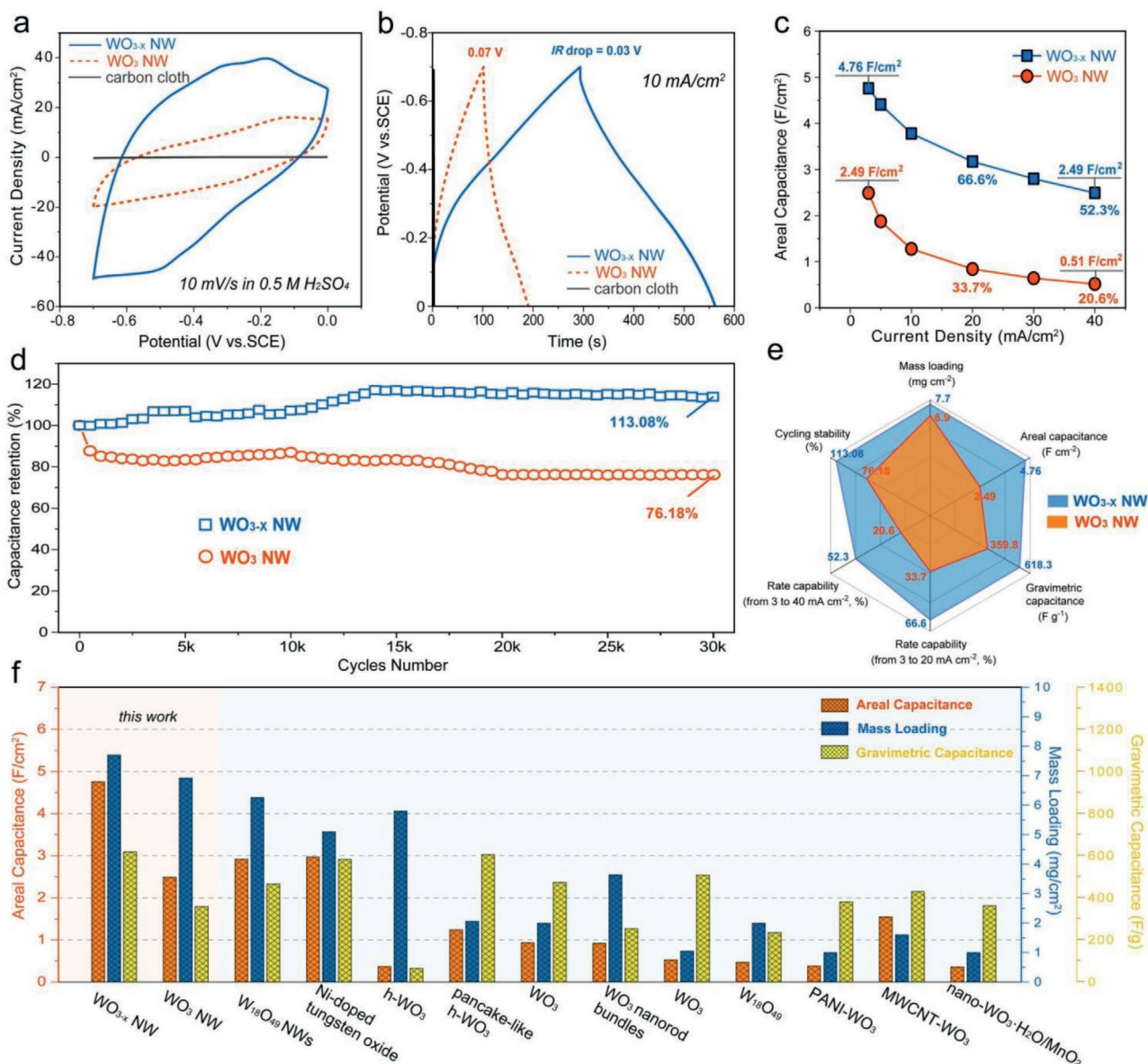


Figure 2. Electrochemistry of WO₃ and oxygen-deficient WO_{3-x} NW electrodes: a) CV profiles measured at 10 mV s⁻¹. b) GCD profiles measured at 10 mA cm⁻². c) Areal capacitance as a function of current density between 3 and 40 mA cm⁻². d) Cycling stability of WO₃ and WO_{3-x} NW. e) The radar chart compares the six figure-of-merits of WO₃ NW (orange) and oxygen-deficient WO_{3-x} NW (blue): mass loading, areal capacitance based on the geometric area, gravimetric capacitance based on the mass of active materials, rate capability (from 3 to 20 and 40 mA cm⁻²) and cycling stability (30 000 cycles). All capacitances are obtained at 3 mA cm⁻². f) A plot compares the areal capacitance, mass loading, and gravimetric capacitance of the oxygen-deficient WO_{3-x} NW electrode with the values of previously reported tungsten oxide-based electrodes (W₁₈O₄₉ NWs,^[11] Ni-doped tungsten oxide,^[12] h-WO₃,^[18a] pancake-like h-WO₃,^[18b] WO₃,^[18c] WO₃ nanorod bundles,^[18d] WO₃,^[18e] W₁₈O₄₉,^[18f] PANI-WO₃,^[18g] MWCNT-WO₃,^[18h] and nano-WO₃-H₂O/MnO₂^[18j]).

its superior capacitive nature. Likewise, the GCD profile of oxygen-deficient WO_{3-x} NW also exhibit a smaller IR drop than that of WO_3 NW. These results show that the introduction of oxygen vacancies cause an increase in the electrical conductivity. Rate capability is an important factor for high performance capacitors. As shown in Figure 2c and Figure S12, Supporting Information, oxygen-deficient WO_{3-x} NW achieved the highest areal capacitance of 4.76 F cm^{-2} (gravimetric capacitance equal to 618 F g^{-1} standardized to 77 mg cm^{-2}) at 3 mA cm^{-2} , which is larger than WO_3 NW (2.49 F cm^{-2} , 359 F g^{-1}). Moreover, the oxygen-deficient WO_{3-x} NW electrode maintains an outstanding rate capability of 66.6% and 52.3% from 3 to 20 and 40 mA cm^{-2} under such high mass loading, respectively, which is 1.8–2.5× higher than WO_3 NW (33.7% and 20.6%, Table S2, Supporting Information). Such results indicate that ion diffusion and charge transfer are extremely effective in WO_{3-x} NW electrode. Even at the high current density of 40 mA cm^{-2} , oxygen-deficient WO_{3-x} NW still can deliver an excellent capacitance of 2.49 F cm^{-2} .

Figure 2d compares the cycling stability of WO_3 and oxygen-deficient WO_{3-x} electrodes evaluated by GCD at 40 mA cm^{-2} . It can be seen that the cycling behavior of oxygen-deficient WO_{3-x} NW is more stable than that of WO_3 . The capacity of oxygen-deficient WO_{3-x} increased slowly in the initial 15 000 cycles, because the electrolyte gradually diffused into the full electrode, which makes it possible to connect more thoroughly. A consistent conservation of capacity is then shown, 113.08% remaining at the 30 000th cycle. In contrast, the WO_3 only retains 76.18% of its capacitance after 30 000 cycles. We collected the SEM images of the tested samples after 30 000th cycle (Figure S13, Supporting Information). The WO_3 sample shows that the active materials in the carbon fiber substrate have apparently peeled, leading to its lower cycling behavior. In contrast, no morphological difference is observed for oxygen-deficient WO_{3-x} NW after cycling; that is, the oxygen-deficient WO_{3-x} structure is retained after the 30 000 cycle stability test. For comparison, we also scraped off the WO_3 active material from WO_3 NW electrode that eliminate sintering effect on the adhesion between carbon cloth and WO_3 , and tested its electrochemical cycling stability. As shown in Figure S14, Supporting Information, upon long-term cycling, the casted WO_3 electrode maintains 77.24% capacitance at the 30000th cycle, similar to the fully oxidized WO_3 NW electrode (76.18%). A radar chart summarizes the electrochemical performance of WO_3 and oxygen-deficient WO_{3-x} electrodes (Figure 2e), that is, mass loading, areal capacitance standardized to geometric surface area, gravimetric capacitance standardized to the mass of active materials, rate capability, and cycling stability. These studies clearly indicate that the oxygen-deficient WO_{3-x} NW has faster kinetics, excellent capacity, and superior cycling stabilization compared with WO_3 , which are the significant features of its application to electrochemical devices. It could be a result of the increased oxygen defects, which increases carrier density and allows faster electron transportation from the current collector to the activity sites in tungsten oxide, resulting in enhanced capacitance and rate capability. Moreover, to the best of our knowledge, the areal capacitance, gravimetric capacitance, and mass loading of oxygen-deficient WO_{3-x} NW significantly outperform the previously reported tungsten oxide-based electrodes (Figure 2f and Table S3, Supporting Information).^[11,12,18]

2.3. Effect of Oxygen Vacancies

The above results reveal that oxygen vacancy plays a critical role in the charge storage ability of the WO_3 materials, leading to better cycling stability, excellent capacity, and faster kinetics comparing with the fully oxidized sample. In this section, we study the interplay between the oxygen vacancies and the structural stability, electrical property, and charge storage capability of the tungsten oxide materials.

To understand the structural features of oxygen-deficient WO_{3-x} NW relevant to its properties, XRD analysis was conducted for oxygen-deficient WO_{3-x} and WO_3 NW. The XRD patterns in Figure 3a show the major reflections of oxygen-deficient WO_{3-x} and WO_3 NW [(100), (001), (200), and (201)]. It can be seen that the peak positions are shifted to lower angles in the oxygen-deficient WO_{3-x} NW. Our DFT calculations also indicate that the W-W distance is expanded from 3.83 to 4.02 Å and from 4.01 to 4.54 Å after forming an O_i vacancy respectively in the hexagonal and orthorhombic structures (Figure 3b), suggesting the relaxation of lattice. The expanded interlayer spacing could enable sufficient electrolyte penetration in the electrode and create further surface area for charge storage, ultimately leading to an increase of capacitance, in excellent agreement with our UV-vis spectra results (Figure S9, Supporting Information) and electrochemical performance, as shown in Figure 2.

To elucidate the relationship between oxygen vacancies and the rate capability, we analyzed the electrochemical impedance spectroscopy (EIS) data of oxygen-deficient WO_{3-x} and WO_3 (Figure 3c). The slope of the WO_{3-x} NW in the middle and low frequencies is closer to 90° as compared to WO_3 , indicating better capacitive behavior of the former.^[19] In addition, as shown in the inset of Figure 3c, WO_{3-x} exhibits much smaller equivalent series resistance (R_s , 0.86 ohm) and charge-transfer resistance (R_{ct}) as compared to that of WO_3 . The existence of oxygen vacancies, which induce an improvement in carrier density (as indicated previously by Mott-Schottky measurements), leads to an improved electrical conductivity property of the WO_{3-x} . The EIS information has been evaluated further by the technique Simon's group have proposed.^[20] We assessed the capacitance models of electrodes by distinguishing the imaginary $C''(\omega)$ and real $C'(\omega)$ part of the whole capacitance $C(\omega)$.^[20,21] The imaginary capacitance $C''(\omega)$ versus frequency is shown in Figure 3d. At the highest $C''(\omega)$ value, the frequency f_0 represents a transition between a capacitive behavior at lower frequency and a resistive behavior at higher frequency for supercapacitors.^[22] The relaxation time τ_0 can be assessed by $\tau_0 = 1/f_0$, which is a reflection of the necessary time to efficiently deliver and store energy.^[23] For the oxygen-deficient WO_{3-x} electrode, the τ_0 value is smaller (3.8 s) than for WO_3 (9.5 s), which demonstrates the former's higher power capability.

More insights into the difference in charge storage kinetics are also provided by CV. Following the formula of $i = a\nu^b$ (i is current density and ν is sweep rate), the power law exponent b is a significant measurement for assessing the charge storage kinetics: $b = 1.0$ indicates an ideal capacitive behavior while $b = 0.5$ demonstrate that the current is controlled by semi-infinite diffusion. In Figure 3e, the $\log(i)$ versus $\log(\nu)$ plot for the cathodic peak at -0.34 V (versus SCE) (Figure 3e, inset) shows

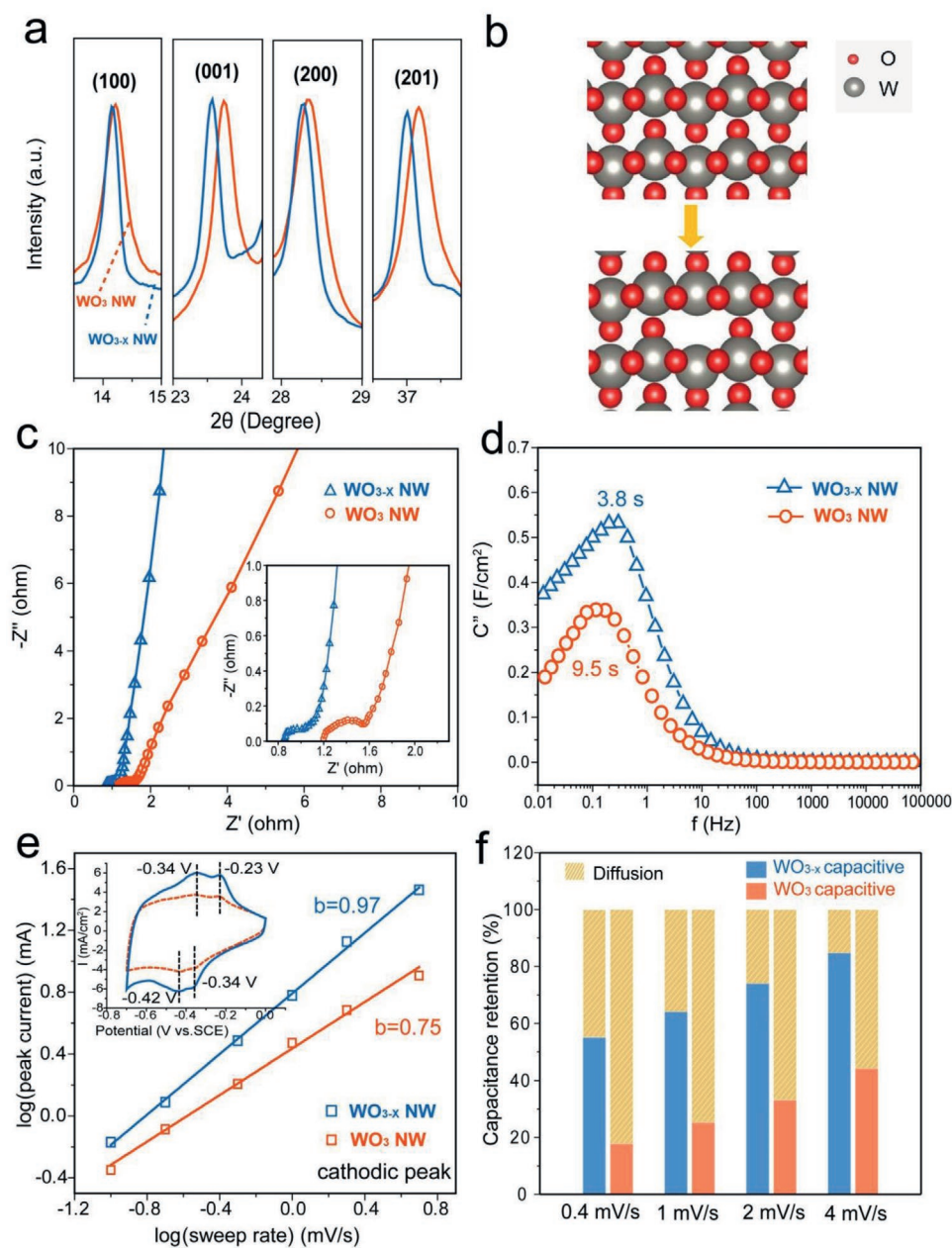


Figure 3. a) Selected XRD patterns of the (100), (001), (200), and (201) diffraction peaks that compare fully oxidized WO_3 and oxygen-deficient WO_{3-x} NWs. The peak location shifts to lower angle that indicates the expansion of the interlayer spacing in oxygen-deficient WO_{3-x} . b) Schematic illustration of the formation of O_i vacancy. Grey and red spheres represent W and O, respectively. c) Nyquist plots of WO_3 and oxygen-deficient WO_{3-x} NW electrodes. d) $C''(\omega)$ versus f plots of WO_3 and WO_{3-x} NW. e) The $\log(i)$ versus $\log(\nu)$ plot of the cathodic current response at -0.34 (versus SCE). Inset showing the CV curves measured at 1 mV s^{-1} of oxygen-deficient WO_{3-x} and WO_3 NW electrodes. f) Histogram image of capacitive capacitance and diffusive capacitance contribution in WO_3 and oxygen-deficient WO_{3-x} .

that the b value of oxygen-deficient WO_{3-x} NW was calculated to be 0.97, suggesting fast charge storage kinetics. In contrast, WO_3 exhibits values of 0.75, which implies that the diffusion processes influence the charge storage. Other cathodic peak and anodic peaks for WO_3 and oxygen-deficient WO_{3-x} show the same general behavior (Figure S15, Supporting Information).

To qualitatively compare the ion diffusion rate in the two electrodes, we measured the diffusion coefficient (D) by

using potentiostatic intermittent titration technology (PITT). Figure S16, Supporting Information shows the transient $I-t$ plots of the oxygen-deficient WO_{3-x} NW and fully oxidized WO_3 NW electrodes collected at -0.3 V versus SCE with a potential step of 10 mV. The rate of current decay is related to the speed of ion diffusion from the electrode/electrolyte interface into the electrode. The $\ln I(t)$ versus t curves was linearly fitted, and the value of D was inversely proportional to the slope of the linear region of $\ln I(t)$ versus t plot. Notably, the oxygen-deficient

WO_{3-x} NW electrode has higher diffusion coefficient value than the WO_3 electrode, supporting that oxygen vacancies enhance the ion diffusion efficiency in the tungsten oxide structure.

The detailed charge storage analyses using the Dunn's method was further separated from capacitive and diffusion-controlled processes (Supporting Information).^[24] The results for the oxygen-deficient WO_{3-x} and WO_3 electrodes are summarized at different scan rates ($0.4\text{--}4\text{ mV s}^{-1}$, Figure 3f). The capacitive contribution of the oxygen-deficient WO_{3-x} was

higher than that of WO_3 at all scan rates. For example, the oxygen-deficient WO_{3-x} exhibits a large capacitive contribution of 74.0% than 33.2% for WO_3 at the representative scanning rate of 2 mV s^{-1} . Capacitive controlled processes generally have fairly fast kinetics than the diffusion-controlled reactions by ion intercalation/de-intercalation in bulk material,^[25] which means a higher contribution from capacitive controlled capacitance, the more capacitance will be storage at ultrafast current densities. Thus, even at high current densities, the oxygen-deficient

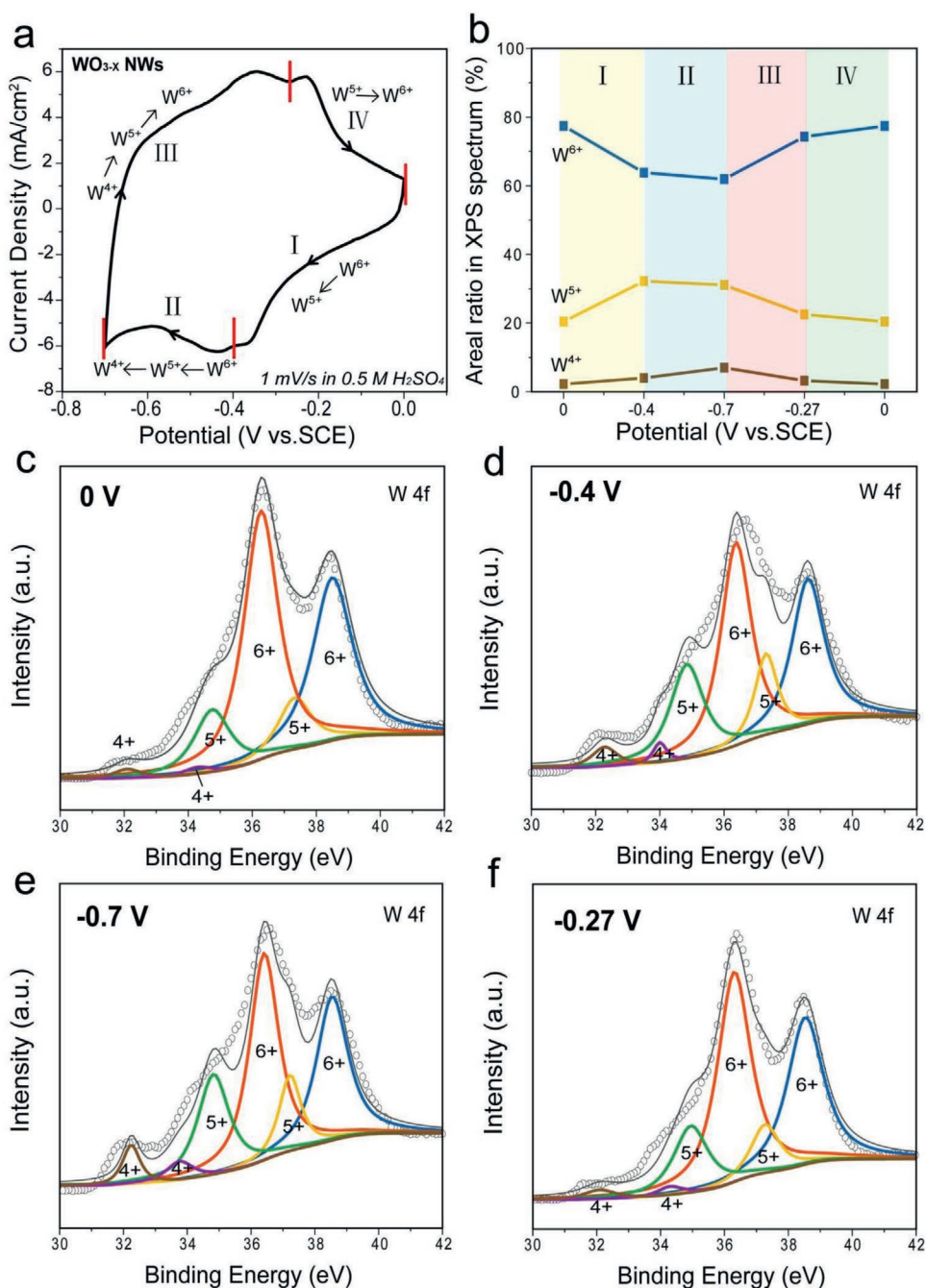


Figure 4. a) CV curve of the WO_{3-x} NW electrode (Arrows highlight the scan direction). b) The plot of areal ratio in XPS spectrum of W^{4+} , W^{5+} , and W^{6+} states as a function of potential. c–f) W 4f core level XPS spectra of the WO_{3-x} NW electrode collected at 0, -0.4, -0.7, and -0.27 V versus SCE.

WO_{3-x} maintains high capacitance and an extraordinary rate capability, as shown in Figure 2c.

The excellent capacitive performance of the oxygen-deficient WO_{3-x} electrode is mainly due to its pseudocapacitive behavior. Therefore, the medium state in oxygen-deficient WO_{3-x} throughout charging/discharging is important for the electrochemical processes of such metal oxides. A series of Ex situ XPS were carried out to study the medium states and charge-storage mechanism of oxygen-deficient WO_{3-x} NW throughout electrochemical charging/discharging processes (Figure 4). We

collected the W 4f XPS of the WO_{3-x} NW electrode at different charging/discharging potentials (0, -0.4, -0.7, and -0.27 V versus SCE) during the CV scans (Figure 4c–f). Figure 4b, and Tables S4, S5, Supporting Information summarize the relative amount of W^{4+} , W^{5+} , and W^{6+} signals. The CV curve can be divided into four steps. Step I with the scan from 0 to -0.4 V, the amount of W^{6+} decreases accompany with substantial increases of W^{5+} , while the relative amount of W^{4+} increase slightly. This indicates that the main reaction involved in step I is corresponding to the reduction of W^{6+} to W^{5+} . When the

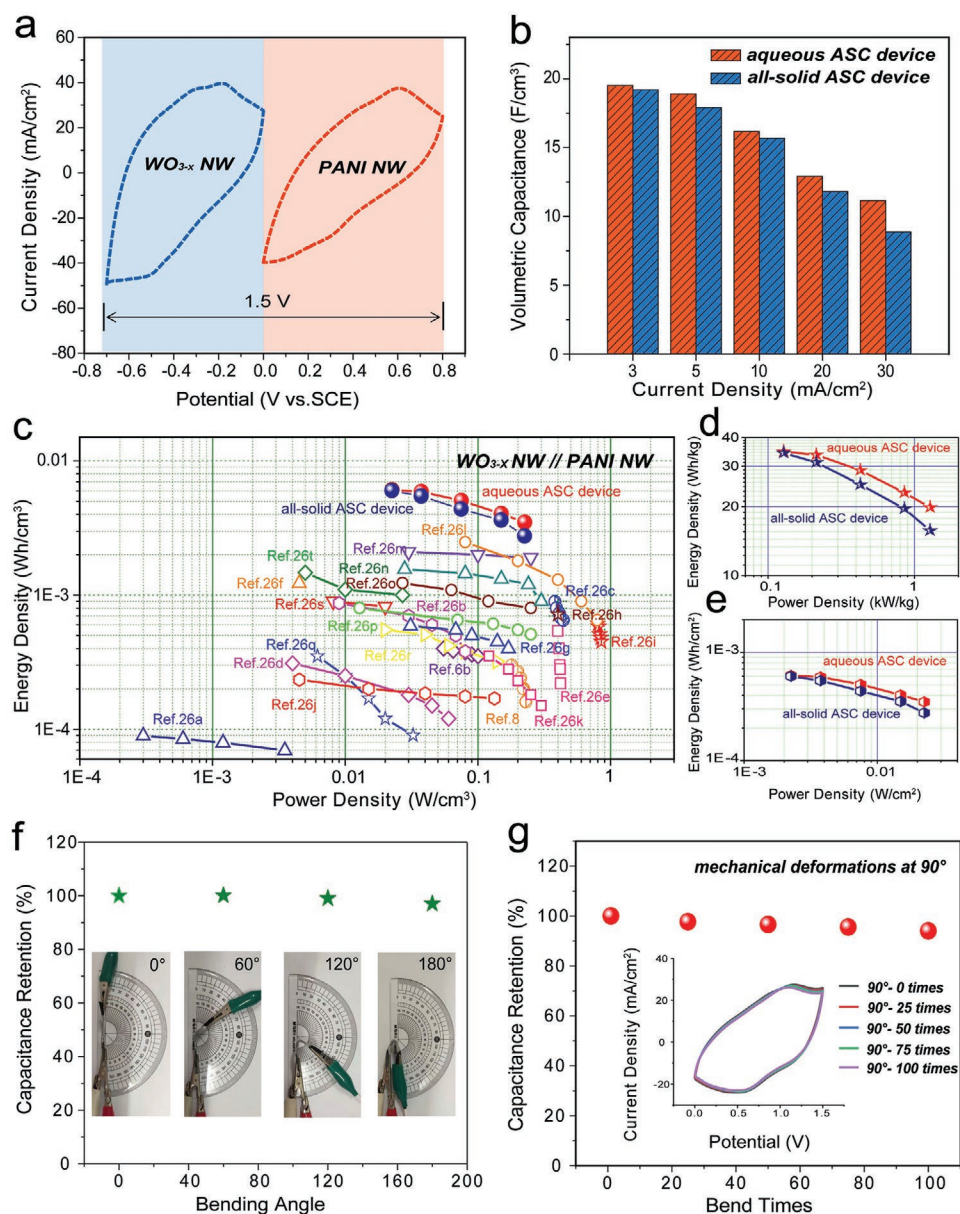


Figure 5. a) CV curves of oxygen-deficient WO_{3-x} and PANI NW electrodes collected at 10 mV s^{-1} . b) Volumetric capacitances of all-solid and aqueous ASCs measured at different current densities. c) Volumetric energy density and power density of the all-solid and aqueous ASC devices and reported devices for comparison. d) Gravimetric energy density and power density of the all-solid and aqueous ASC devices. e) Areal energy density and power density of the all-solid and aqueous ASC devices. f) Capacitance retention of the WO_{3-x} NW//PANI NW ASC collected at different bend angles. g) Capacitance retention under repeated mechanical deformations at bending angle of 90° . Inset showing the CVs obtained after folding at 90° for 25, 50, 75, and 100 times.

potential reached -0.7 V, the amount of W^{6+} continue decreases (step II). At the same time, W^{5+} also decrease with the increase of W^{4+} , indicating there is a transformation among W^{6+} , W^{5+} and W^{4+} . At step III and IV, the W^{4+} states were converted back to W^{5+} and then W^{6+} during the reverse scan. Significantly, the symmetrical variation of the tungsten oxidation states during the scan confirmed the reactions occurred on the WO_{3-x} NW electrode surface are highly reversible, which is important for pseudocapacitive electrode. These *Ex-situ* XPS analysis illustrate that the mechanism of charge storage in WO_{3-x} NW involves the reversible redox of W^{4+} , W^{5+} , and W^{6+} states, which is critical to the cycling stability and capacitive performance.

2.4. Asymmetric Electrochemical Capacitors

Asymmetric electrochemical capacitors were fabricated by assembling a WO_{3-x} NW anode and a polyaniline nanowire (PANI NW) cathode. H_2SO_4/PVA was used as the electrolyte for the all-solid ASC, whereas the 0.5 M H_2SO_4 solution was used for the aqueous ASC. Structural, morphological, and electrochemical characterizations of the PANI NW are summarized in Figures S17, S18, Supporting Information. Figure 5a shows CV profiles of WO_{3-x} NW (-0.7 to 0 V) and PANI NW (0 to 0.8 V) at 10 mV s^{-1} , which in combination generated a large voltage window up to 1.5 V. With the increase of sweep rate, the CV curves don't show significant distortion, indicating that the ASC device has an outstanding rate capability (Figure S19, Supporting Information). The symmetric and linear curves of the all-solid and aqueous ASCs demonstrate an ideal capacitive behavior (Figures S20, S21, Supporting Information). The ASC devices show outstanding volumetric capacitance of 19.5 (aqueous) and 19.2 F cm^{-3} (all-solid) at 3 mA cm^{-2} (Figure 5b). More importantly, our device is stable with capacitance retention of 95% after 5000 cycles (Figure S22, Supporting Information). Benefiting from the high voltage and large capacitance, our aqueous and all-solid ASCs show the highest performance. The all-solid ASC exhibit a volumetric energy density of 6.0 mWh cm^{-3} at a power density of 22.5 and 2.76 mWh cm^{-3} at 225 mW cm^{-3} , while the aqueous ASC shows a volumetric energy density of 6.1 mWh cm^{-3} at a power density of 22.5 mW cm^{-3} and 3.48 mWh cm^{-3} at 225 mW cm^{-3} . All results are better than those of other supercapacitor devices (inset of Figure 5c).^{18,26]} We have also calculated the gravimetric energy density and areal energy density of the aqueous and all-solid ASC devices (Figure 5d,e). Our devices show a specific energy density of 34.7 Wh kg^{-1} at the power density of 0.13 kW kg^{-1} for the aqueous ASC or 34.2 Wh kg^{-1} at 0.13 kW kg^{-1} for the all-solid one. Our devices show areal energy density of 0.61 mWh cm^{-2} at the power density of 2.25 mW cm^{-2} for the aqueous ASC or 0.6 mWh cm^{-2} at 2.25 mW cm^{-2} for the all-solid one.

Moreover, our all-solid ASC device can be bent without deteriorating their capacities under different deformation conditions (different bending angels and twisted status), indicative of its superior flexibility (Figure 5f, Figures S23, S24, Supporting Information). The electrochemical performance of the all-solid ASC undergo mechanical deformation was tested by folding it at 90° for $100\times$. Encouragingly, there is no obvious capacity sacrifice ($>95\%$ retention) under the repeated mechanical bending

of the all-solid ASC (Figure 5g), revealing its excellent mechanical strength. As a demonstration, a red light-emitting diode (LED) or an electrical fan was operated by two ASC devices linked in series, demonstrating its potential for practical applications (Figure S25, Supporting Information).

3. Conclusion

In summary, we have demonstrated that the implementation of oxygen vacancies into WO_3 leads to significantly improved electrical conductivity and electrochemical properties. These oxygen vacancies increase the carrier density, which facilitates faster electron transport. Meanwhile, the oxygen-deficient WO_{3-x} NW with an increased interlayer spacing ensure ion migration throughout the entire material, leading to a maximized material utilization for energy storage with a mass loading up to 77 mg cm^{-2} . The oxygen-deficient WO_{3-x} NW shows substantially improved rate capability as compared to WO_3 . The enhanced rate capability of the oxygen-deficient WO_{3-x} NW is attributed to the improved charge storage kinetics in the bulk material. The current strategy represents a promising attempt to promote the pseudocapacitive charge storage property of redox-active materials.

Supporting Information

Supporting Information is available from the Wiley Online Library or from the author.

Acknowledgements

Z.-H.H. and H.L. contributed equally to this work. This work was supported by National Natural Science Foundation of China (No. 52071171), Liaoning Revitalization Talents Program – Pan Deng Scholars (XLYC1802005), Liaoning BaiQianWan Talents Program (LNBQW2018B0048), National Science Fund of Liaoning Province for Excellent Young Scholars (2019-YQ-04), Key Project of Scientific Research of the Education Department of Liaoning Province (LZD201902), General Project of Scientific Research of the Education Department of Liaoning Province (LJC201905), Research Fund for the Doctoral Program of Liaoning Province (2019-BS-112), Foundation for Young Scholars of Liaoning University (LDQN2019006). The calculations done at the University of Texas at Austin were supported by the Welch Foundation (F-1841) and the Texas Advanced Computing Center.

Conflict of Interest

The authors declare no conflict of interest.

Keywords

charge storage kinetics, electrochemical capacitors, high-performance, oxygen vacancies, tungsten oxide

Received: August 3, 2020

Revised: November 1, 2020

Published online: December 2, 2020

- [1] a) L. Shen, L. Du, S. Tan, Z. Zang, C. Zhao, W. Mai, *Chem. Commun.* **2016**, 52, 6296; b) C. Jo, J. Hwang, H. Song, A. H. Dao, Y. T. Kim, S. H. Lee, S. W. Hong, S. Yoon, J. Lee, *Adv. Funct. Mater.* **2013**, 23, 3747; c) J. C. Liu, H. Li, M. Batmunkh, X. Xiao, Y. Sun, Q. Zhao, X. Liu, Z. H. Huang, T. Y. Ma, *J. Mater. Chem. A* **2019**, 7, 23941; d) J. C. Liu, Z. H. Huang, T. Y. Ma, *Small Struct.* **2020**, 2000020; e) M. S. Balogun, H. Yang, Y. Luo, W. Qiu, Y. Huang, Z. Q. Liu, Y. Tong, *Energy Environ. Sci.* **2018**, 11, 1859; f) Z. H. Huang, Y. Song, X. X. Liu, *Chem. Eng. J.* **2019**, 358, 1529; g) X. Huang, H. Liu, X. Zhang, H. Jiang, *ACS Appl. Mater. Interfaces* **2015**, 7, 27845; h) X. X. Li, X. H. Deng, Q. J. Li, S. Huang, K. Xiao, Z. Q. Liu, Y. Tong, *Electrochim. Acta* **2018**, 264, 46.
- [2] Z. H. Huang, Y. Song, D. Y. Feng, Z. Sun, X. Sun, X. X. Liu, *ACS Nano* **2018**, 12, 3557.
- [3] G. Wang, Y. Yang, D. Han, Y. Li, *Nano Today* **2017**, 13, 23.
- [4] H. Zheng, J. Z. Ou, M. S. Strano, R. B. Kaner, A. Mitchell, K. Kalantar-zadeh, *Adv. Funct. Mater.* **2011**, 21, 2175.
- [5] G. Wang, Y. Yang, Y. Ling, H. Wang, X. Lu, Y. C. Pu, J. Z. Zhang, Y. Tong, Y. Li, *J. Mater. Chem. A* **2016**, 4, 2849.
- [6] a) X. Lu, G. Wang, T. Zhai, M. Yu, J. Gan, Y. Tong, Y. Li, *Nano Lett.* **2012**, 12, 1690; b) X. Lu, Y. Zeng, M. Yu, T. Zhai, C. Liang, S. Xie, M. S. Balogun, Y. Tong, *Adv. Mater.* **2014**, 26, 3148; c) P. Yang, X. Xiao, Y. Li, Y. Ding, P. Qiang, X. Tan, W. Mai, Z. Lin, W. Wu, T. Li, H. Jin, P. Liu, J. Zhou, C. P. Wong, Z. L. Wang, *ACS Nano* **2013**, 7, 2617; d) T. Zhai, S. Xie, M. Yu, P. Fang, C. Liang, X. Lu, Y. Tong, *Nano Energy* **2014**, 8, 255; e) H. Wu, C. Xu, J. Xu, L. Lu, Z. Fan, X. Chen, Y. Song, D. Li, *Nanotechnology* **2013**, 24, 455401; f) S. Balendhran, J. Deng, J. Z. Ou, S. Walia, J. Scott, J. Tang, K. L. Wang, M. R. Field, S. Russo, S. Zhuiykov, M. S. Strano, N. Medhekar, S. Sriram, M. Bhaskaran, K. Kalantar-zadeh, *Adv. Mater.* **2013**, 25, 109; g) X. K. Hu, Y. T. Qian, Z. T. Song, J. R. Huang, R. Cao, J. Q. Xiao, *Chem. Mater.* **2008**, 20, 1527; h) M. Dieterle, G. Weinberg, G. Mestl, *Phys. Chem. Chem. Phys.* **2002**, 4, 812; i) G. Wang, Y. Ling, Y. Li, *Nanoscale* **2012**, 4, 6682.
- [7] a) C. Yao, B. Wei, H. Li, G. Wang, Q. Han, H. Ma, Q. Gong, *J. Mater. Chem. A* **2017**, 5, 56; b) Y. Song, T. Y. Liu, B. Yao, T. Y. Kou, D. Y. Feng, X. X. Liu, Y. Li, *Small* **2017**, 13, 1700067; c) H. S. Kim, J. B. Cook, H. Lin, J. S. Ko, S. H. Tolbert, V. Ozolins, B. Dunn, *Nature Mater.* **2017**, 16, 454.
- [8] X. H. Lu, M. H. Yu, G. M. Wang, T. Zhai, S. L. Xie, Y. C. Ling, Y. X. Tong, Y. Li, *Adv. Mater.* **2013**, 25, 267.
- [9] H. Wang, R. Fan, J. Miao, J. Chen, S. Mao, J. Deng, Y. Wang, *J. Mater. Chem. A* **2018**, 6, 6780.
- [10] a) Z. Gu, H. Li, T. Zhai, W. Yang, Y. Xia, Y. Ma, J. Yao, *J. Solid State Chem.* **2007**, 180, 98; b) S. Yao, X. Zheng, X. Zhang, H. Xiao, F. Qu, X. Wu, *Mater. Lett.* **2017**, 186, 94; c) J. Chu, D. Lu, X. Wang, X. Wang, S. Xiong, *J. Alloys Compd.* **2017**, 702, 568; d) M. Zhu, Y. Huang, Y. Huang, Z. Pei, Q. Xue, H. Li, H. Geng, C. Zhi, *Adv. Funct. Mater.* **2016**, 26, 4481; e) P. A. Shinde, A. C. Lokhande, N. R. Chodankar, A. M. Patil, J. H. Kim, C. D. Lokhande, *Electrochim. Acta* **2017**, 224, 397.
- [11] K. Li, Y. Shao, S. Liu, Q. Zhang, H. Wang, Y. Li, R. B. Kaner, *Small* **2017**, 13, 1700380.
- [12] T. Meng, Z. Kou, I. S. Amiinu, X. Hong, Q. Li, Y. Tang, Y. Zhao, S. Liu, L. Mai, S. Mu, *Small* **2018**, 14, 1800381.
- [13] a) C. Han, D. Wang, Q. Li, Z. Xing, X. Yang, *ACS Appl. Energy Mater.* **2019**, 2, 2409; b) K. Qian, L. Du, X. Zhu, S. Liang, S. Chen, H. Kobayashi, X. Yan, M. Xu, Y. Dai, R. Li, *J. Mater. Chem. A* **2019**, 7, 14592; c) L. Cao, Y. Li, J. Wu, W. Li, J. Huang, Y. Feng, C. Yao, J. Li, R. Wang, Q. Kang, L. Feng, *J. Alloys Compd.* **2018**, 744, 672.
- [14] a) G. Wang, H. Wang, Y. Ling, Y. Tang, X. Yang, R. C. Fitzmorris, C. Wang, J. Z. Zhang, Y. Li, *Nano Lett.* **2011**, 11, 3026; b) D. Liu, Y. Zhang, P. Xiao, B. B. Garcia, Q. Zhang, X. Zhou, Y. H. Jeong, G. Cao, *Electrochim. Acta* **2009**, 54, 6816.
- [15] F. Wang, C. D. Valentin, G. Pacchioni, *Phys. Rev. B* **2011**, 84, 073103.
- [16] The Materials Project, <https://materialsproject.org/> (accessed: September 2020).
- [17] R. Chatten, A. V. Chadwick, A. Rougier, P. J. Lindan, *J. Phys. Chem. B* **2005**, 109, 3146.
- [18] a) S. H. Ji, N. R. Chodankar, W. S. Jang, D. H. Kim, *Electrochim. Acta* **2019**, 299, 245; b) J. Jia, X. Liu, R. Mi, N. Liu, Z. Xiong, L. Yuan, C. Wang, G. Sheng, L. Cao, X. Zhou, X. Liu, *J. Mater. Chem. A* **2018**, 6, 15330; c) J. Chen, H. Wang, J. Deng, C. Xu, Y. Wang, *J. Mater. Chem. A* **2018**, 6, 8986; d) H. Peng, G. Ma, K. Sun, J. Mu, M. Luo, *Z. Lei, Electrochim. Acta* **2014**, 147, 54; e) D. Mandal, P. Routh, A. K. Nandi, *Small* **2017**, 14, 1702881; f) S. Parh, H. W. Shim, C. W. Lee, H. J. Song, J. C. Kim, D. W. Kim, *Nano Res.* **2016**, 9, 633; g) J. W. Geng, Y. J. Ye, D. Guo, X. X. Liu, *J. Power Sources* **2017**, 342, 980; h) P. A. Shinde, Y. Seo, C. Ray, S. C. Jun, *Electrochim. Acta* **2019**, 308, 231; i) C. Yuan, H. Lin, H. Lu, E. Xing, Y. Zhang, B. Xie, *Mater. Lett.* **2015**, 148, 167.
- [19] a) Z. H. Huang, F. F. Sun, M. Batmunkh, W. H. Li, H. Li, Y. Sun, Q. Zhao, X. Liu, T. Y. Ma, *J. Mater. Chem. A* **2019**, 7, 11826; b) X. Cai, Y. Song, Z. Sun, D. Guo, X. X. Liu, *J. Power Sources* **2017**, 365, 126; c) Z. H. Huang, T. Y. Liu, Y. Song, Y. Li, X. X. Liu, *Nanoscale* **2017**, 9, 13119.
- [20] P. C. Gao, W. Y. Tsai, B. Daffos, P. L. Taberna, C. R. Perez, Y. Gogotsi, P. Simon, F. Favier, *Nano Energy* **2015**, 12, 197.
- [21] P. L. Taberna, P. Simon, J. F. Fauvarque, *J. Electrochem. Soc.* **2003**, 150, A292.
- [22] S. Q. Wang, X. Cai, Y. Song, X. Sun, X. X. Liu, *Adv. Funct. Mater.* **2018**, 28, 1803901.
- [23] M. Yu, S. Zhao, H. Feng, L. Hu, X. Zhang, Y. Zeng, Y. Tong, X. Lu, *ACS Energy Lett.* **2017**, 2, 1862.
- [24] a) S. Ardizzone, G. Fregonara, S. Trasatti, *Electrochim. Acta* **1990**, 35, 263; b) J. Duay, S. A. Sherrill, Z. Gui, E. Gillette, S. B. Lee, *ACS Nano* **2013**, 7, 1200.
- [25] a) F. Bonaccorso, L. Colombo, G. Yu, M. Stoller, V. Tozzini, A. C. Ferrari, R. S. Ruoff, V. Pellegrini, *Science* **2015**, 347, 1246501; b) Y. Song, T. Liu, B. Yao, M. Li, T. Kou, Z. H. Huang, D. Y. Feng, F. Wang, Y. Tong, X. X. Liu, Y. Li, *ACS Energy Lett.* **2017**, 2, 1752.
- [26] a) F. M. Wang, Y. C. Li, Z. Z. Cheng, K. Xu, X. Y. Zhan, Z. X. Wang, J. He, *Phys. Chem. Chem. Phys.* **2014**, 16, 12214; b) T. Zhai, X. Lu, Y. Ling, M. Yu, G. Wang, T. Liu, C. Liang, Y. Tong, Y. Li, *Adv. Mater.* **2014**, 26, 5869; c) Y. Zeng, Y. Han, Y. Zhao, Y. Zeng, M. Yu, Y. Liu, H. Tang, Y. Tong, X. Lu, *Adv. Energy Mater.* **2015**, 5, 1402176; d) Q. Tang, M. Chen, C. Yang, W. Wang, H. Bao, G. Wang, *ACS Appl. Mater. Interfaces* **2015**, 7, 15303; e) X. Xiao, X. Peng, H. Jin, T. Li, C. Zhang, B. Gao, B. Hu, K. Huo, J. Zhou, *Adv. Mater.* **2013**, 25, 5091; f) Z. Zhang, K. Chi, F. Xiao, S. Wang, *J. Mater. Chem. A* **2015**, 3, 12828; g) P. Sun, Z. Deng, P. Yang, X. Yu, Y. Chen, Z. Liang, H. Meng, W. Xie, S. Tan, W. Mai, *J. Mater. Chem. A* **2015**, 3, 12076; h) T. Zhai, F. Wang, M. Yu, S. Xie, C. Liang, C. Li, F. Xiao, R. Tang, Q. Wu, X. Lu, Y. Tong, *Nanoscale* **2013**, 5, 6790; i) X. Lu, M. Yu, T. Zhai, G. Wang, S. Xie, T. Liu, C. Liang, Y. Tong, Y. Li, *Nano Lett.* **2013**, 13, 2628; j) W. Zilong, Z. Zhu, J. Qiu, S. Yang, *J. Mater. Chem. C* **2014**, 2, 1331; k) X. F. Lu, X. Y. Chen, W. Zhou, Y. X. Tong, G. R. Li, *ACS Appl. Mater. Interfaces* **2015**, 7, 14843; l) J. X. Feng, S. H. Ye, A. L. Wang, X. F. Lu, Y. X. Tong, G. R. Li, *Adv. Funct. Mater.* **2014**, 24, 3535; m) L. Hua, Z. Ma, P. Shi, L. Li, K. Rui, J. Zhou, X. Huang, X. Liu, J. Zhu, G. Sun, W. Huang, *J. Mater. Chem. A* **2017**, 5, 2483; n) R. Li, Y. Wang, C. Zhou, C. Wang, X. Ba, Y. Li, X. Huang, J. Liu, *Adv. Funct. Mater.* **2015**, 25, 5384; o) Z. Zhang, F. Xiao, J. Xiao, S. Wang, *J. Mater. Chem. A* **2015**, 3, 11817; p) D. Y. Feng, Y. Song, Z. H. Huang, X. X. Xu, X. X. Liu, *J. Power Sources* **2016**, 324, 788; q) J. X. Feng, S. H. Ye, X. F. Lu, Y. X. Tong, G. R. Li, *ACS Appl. Mater. Interfaces* **2015**, 7, 11444; r) P. Yang, Y. Ding, Z. Lin, Z. Chen, Y. Li, P. Qiang, M. Ebrahimi, W. Mai, C. P. Wong, Z. L. Wang, *Nano Lett.* **2014**, 14, 731; s) Z. Zhang, F. Xiao, S. Wang, *J. Mater. Chem. A* **2015**, 3, 11215; t) G. Yilmaz, C. X. Guo, X. Lu, *ChemElectroChem* **2016**, 3, 158.